Proceedings of the
Annual Stability Conference
Structural Stability Research Council
Atlanta, Georgia, April 21-24, 2020

Large-scale experimental lateral-torsional buckling tests of welded I-section members

Ryan Slein[1], Joshua S. Buth[2], Wajahat Latif[3], Ajit M. Kamath[4], Ammar A. Alshannaq[5], Ryan J. Sherman[6], David W. Scott[7], Donald W. White[8]

Abstract

The AISC 360 *Specification* Chapter F I-section member flexural resistance equations are a central part of structural steel design in the United States. The "unified" provisions of Sections F4 and F5 address general singly and doubly symmetric I-section members. Analytical studies and experimental tests subsequent to the implementation of these provisions within the 2005 AISC *Specification* suggest that the corresponding inelastic lateral-torsional buckling (LTB) and tension flange yielding (TFY) resistance equations can be improved, resulting in significantly larger predicted strengths in certain cases and somewhat smaller predicted strengths in other cases. Twelve large-scale specimens are being tested at the Georgia Institute of Technology to further investigate these predictions. The broad objective is to achieve a target reliability index of $\beta = 2.6$, or close to this value, for building design at a live-to-dead load ratio of 3.0 throughout the design space involving all types of statically determinate I-section flexural members. This paper discusses the design of these tests, including the details of how the test fixtures and bracing systems are configured to minimize incidental restraint. The paper discusses the validation of the testing system by comparison of elastic buckling experimental results to analytical and numerical solutions.

1. Introduction

The AISC *Specification* Chapter F equations provide a broad characterization of the flexural resistance of all types of I-section members, including rolled and welded members, members with doubly and singly symmetric cross-section profiles, and members with compact, noncompact or slender flanges and/or webs, failing by plastic, inelastic, or elastic lateral-torsional buckling (LTB). Closely related equations exist within AASHTO (2017) LRFD *Specifications* for steel bridge design and in AISC Design Guide 25 (White and Jeong, 2020) for web-tapered and other nonprismatic I-section members.

[1] Graduate Research Assistant, Georgia Institute of Technology, <ryan.slein@gatech.edu>
[2] Civil Engineer II, Georgia Department of Transportation, <JButh@dot.ga.gov>
[3] Graduate Research Assistant, Georgia Institute of Technology, <wlatif@gatech.edu>
[4] Graduate Research Assistant, Georgia Institute of Technology, <ajit.kamath@gatech.edu>
[5] Graduate Research Assistant, Georgia Institute of Technology, <aalshannaq@gatech.edu>
[6] Assistant Professor, Georgia Institute of Technology, <ryan.sherman@ce.gatech.edu>
[7] Professor and Chair, Dept.of Civil Eng. and Constr., Georgia Southern University, <dscott@georgiasouthern.edu>
[8] Professor, Georgia Institute of Technology, <dwhite@ce.gatech.edu>

Twelve large-scale specimens are being tested at the Georgia Institute of Technology, targeting fundamental evaluation and characterization of the LTB resistance of welded I-section members subjected to flexure. The primary objectives of the research are to:

1) Improve the definition of the anchor points (L_p, $M_{n.CFY}$) and (L_r, M_{rx}) pertaining to the AISC *Specification* Section F4 and F5 inelastic LTB resistance equations, where L_p is the limiting unbraced length for the limit state of compression flange yielding under uniform bending, $M_{n.CFY}$ is the corresponding compression flange yielding (or "plateau") flexural resistance, L_r is the limiting unbraced length for the limit state of inelastic LTB, and M_{rx} is the uniform bending flexural resistance corresponding to L_r.
2) Enhance the AISC *Specification* Section F4 and F5 tension flange yielding (TFY) provisions, specifically eliminate the current TFY limit state provisions, and allow for development of significant reserve capacity involving yielding in flexural tension by incorporating early tension yielding effects into the calculation of the cross-section yield moment to the compression flange, M_{yc}.

There is clear evidence based on the research conducted to date that opportunities exist to realize substantially larger resistances in certain areas of the design space, while in other areas, the calculated resistances need to be reduced a small extent to realize a target reliability index of $\beta = 2.6$ in building design at a live-to-dead load ratio of 3.0.

This paper discusses the design of the 12 tests to achieve the above objectives, then focuses on the validation of the corresponding testing configuration. Lateral-torsional buckling test results can be sensitive to incidental restraint in the testing configuration (Ziemian 2010). The testing configuration described in this paper utilizes Polytetrafluoroethylene (PTFE) coated spherical bearings for multi-rotational degree-of-freedom releases, mechanical bearings for the single rotational degree-of-freedom releases (as part of a Watt's Linkage bracing system), and lubricated roller packs for single translational degree-of-freedom releases. The effectiveness of these "releases" of rotational and translational constraint is evaluated directly by testing a specimen in the elastic LTB range and comparing the measured responses to various analytical and numerical solutions.

2. Background

Relatively comprehensive assessments of analytical studies and experimental test results conducted to date have raised concerns that the AISC Section F4 and F5 flexural resistance provisions may not satisfy accepted target reliability indices in certain cases pertaining to the LTB of I-section members (Subramanian et al. 2018; Subramanian and White 2017). However, the experimental test data is quite sparse within a number of "regions" of the corresponding design space. Quality experimental data is critical for the validation of refined shell finite element analysis (FEA) procedures that can be employed to investigate the flexural resistances within the design space more comprehensively.

One way of quantifying the LTB slenderness of general I-section members is the normalized slenderness parameter

$$c = \left(KL_b \sqrt{F_{yc} / E} \right) / r_t \tag{1}$$

where K is an LTB effective length factor, L_b is the unbraced length of the critical unbraced length, F_{yc} is the yield stress of the compression flange, E is the elastic modulus, and r_t is the radius of gyration defined by AISC Chapter F. White and Jung (2004) and White and Kim (2004) compiled a database of results from a large number of LTB experimental tests that have been performed throughout the world, emphasizing the predictions of the test results by the AISC (2005) Section F4 and F5 provisions. Subramanian et al. (2018) reevaluated the results from this database, including a number of new tests and utilizing more rigorous LTB effective length factor calculations. Figure 1 and 2 summarize the results for with M_{test}/M_n versus the normalized slenderness parameter defined by EQ. 1 for the moment gradient and constant moment LTB tests considered by Subramanian et al. (2018), respectively.

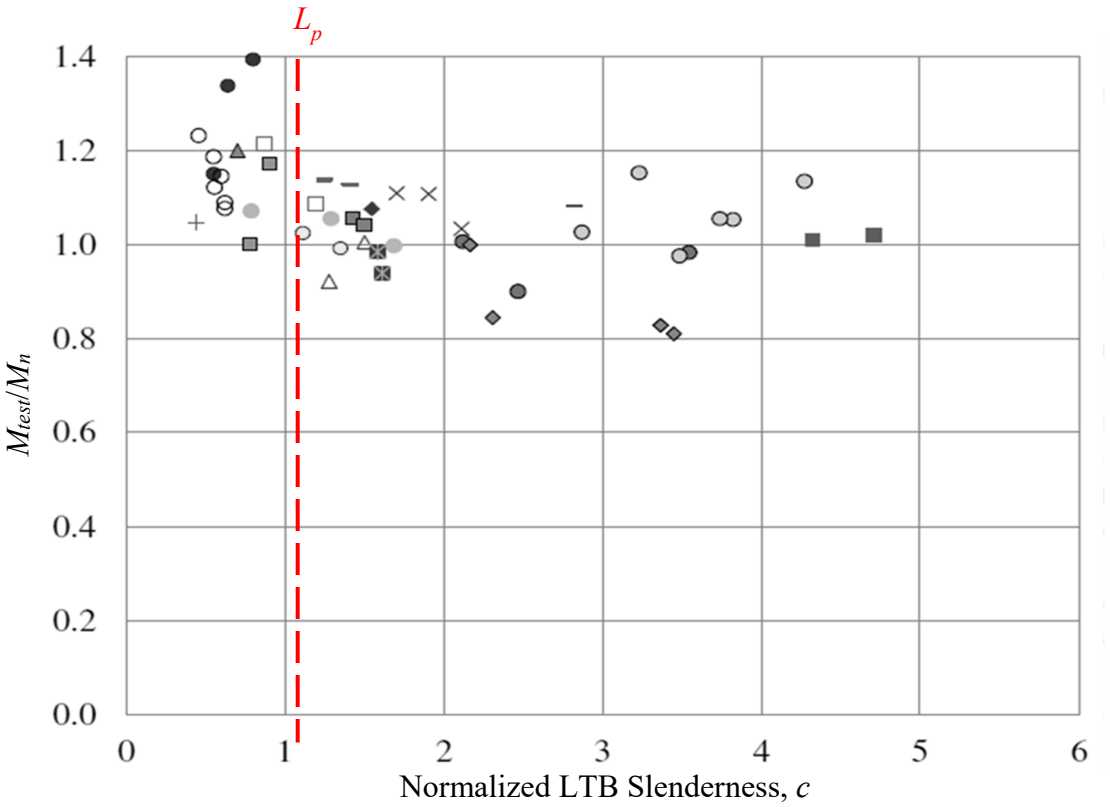

Figure 1: Moment gradient LTB experimental tests considered by Subramanian et al. (2018).

Figs. 1 and 2 show a dashed vertical line at c = 1.1; this c value corresponds to the coefficient of 1.1 in the AISC (2016) Section F4 and F5 definition of L_p. The length L_r within the slender web member provisions of Section F5 correspond to c = 3.75. For noncompact and compact web members, the c value corresponding to L_r is generally larger than 3.75. All of the data points shown in Figs. 1 and 2 fall within, or in a few cases, slightly outside of the inelastic LTB range bounded by L_p and L_r. Designs in the final constructed condition often fall between L_p and L_r; therefore, the inelastic buckling range is of the significant importance in practice. Considering Figs. 1 and 2, there are a significant number of tests within each web slenderness classification for $c \leq 1.1$, although these figures do not show the web slenderness classification directly. Between $1.1 < c \leq 2$, there is also a significant number of tests within each web slenderness classification. However, for $c > 2$, there are a number of ranges of LTB and web slenderness where the data is sparse or

nonexistent. Also, it is important to note that the tests conducted in the inelastic LTB range generally tend to have lower M_{test}/M_n than the tests in the plastic LTB range (i.e., $c \leq 1.1$).

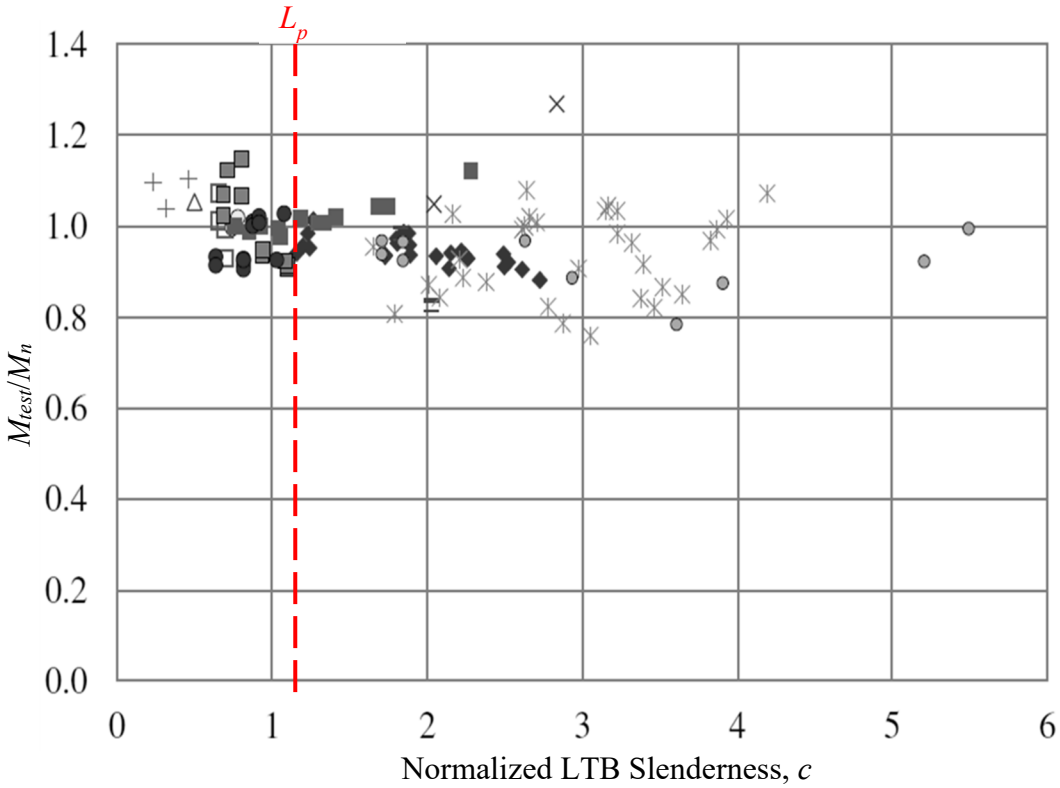

Figure 2: Constant moment LTB experimental tests considered by Subramanian et al. (2018).

Tables 1 and 2 list the total number of tests conducted per web classification within the different ranges of the LTB slenderness parameter, excluding and including the new tests being conducted at Georgia Tech. A design matrix of the new LTB test specimens is provided in Table 3.

Table 1: Number of moment gradient LTB tests conducted per web and lateral-torsional buckling slenderness classification, before and after the Georgia Tech tests are included.

	Normalized LTB Slenderness, *c*		
Web	**2 to 3**	**3 to 4**	**4 <**
Compact	1 → **2**	4	3
Noncompact	0 → **2**	0 → **2**	0
Slender	6	3	0

Table 2: Number of constant moment LTB tests conducted per web and lateral-torsional buckling slenderness classification, before and after the Georgia Tech tests are included.

	Normalized LTB Slenderness, *c*		
Web	**2 to 3**	**3 to 4**	**4 <**
Compact	18	10	2
Noncompact	4	0 → **2**	0
Slender	11	6	1 → **2**

Table 3: Design matrix of new LTB test specimens*.

Test #	Web	L_b	Flange PL†	Web PL	c	K	KL_b/r_t	C_b	R_{pc} or R_{pg}
1	Compact	8.5	6x3/8	18x1/4	2.68	0.88	59	1.17	1.15
2	Noncompact	8.5	6x3/8	22x3/16	2.69	0.89	59	1.17	1.03
3	Noncompact	8.5	6x3/8	22x3/16	2.71	0.90	60	1.17	1.03
4	Noncompact	10	5x5/16	20x3/16	3.85	0.87	85	1.18	1.04
5	Noncompact/ Slender	8.5	5x5/16	30x1/4	3.85	0.90	85	1.17	1.00
6	Noncompact	10.5	5x5/16	20x3/16	3.85	0.83	85	1.00	1.04
7	Noncompact	13	6x3/8	22x3/16	3.98	0.86	87	1.00	1.03
8	Slender	11.5	5x5/16	28x3/16	4.72	0.88	104	1.00	0.93

* Specimen designs conducted assuming a static yield strength of the plates of F_y = 60 ksi; units for L_b are in ft., all other dimensions are in units of inches

† $b_f/2t_f$ = 8.0, all tests

The second thrust of this research is to eliminate the current tension flange yielding limit state check through the calculation of a more mechanistically sound compression flange yield moment, M_{yc}. In the AISC (2016) provisions, the TFY check limits the nominal capacity of slender web members to the nominal onset of yielding of the tension flange. This check may govern when the cross-section is singly-symmetric and the section modulus to the extreme tension fiber, S_{xt}, is smaller than the section modulus to the extreme compression fiber, S_{xc}. In this case, the tension flange yield moment, M_{yt}, is based on the stress profile shown in Fig. 3a. The current AISC (2016) calculation of the compression flange yield moment is based on the stress profile of Fig. 3b, where the section is assumed to remain elastic up to the development of the initial compressive yield, even though tension yield has occurred well before this stage.

The nominal capacity of the section is capped by the TFY limit state before the large tensile strain is ever reached; however, the equations correspond to these intermediate stress profiles. The TFY limit state calculations can be eliminated by capturing the tension yielding effects within the actual stress profile at the development of the "true M_{yc}," as shown in Fig. 3c. This profile can be calculated using either strain compatibility, which is employed frequently in concrete design, or for homogeneous singly-symmetric I-sections, via a closed-form equation.

Table 4 lists four additional specimens being tested at Georgia Tech. They all employ the cross-section shown in Fig. 3. These tests involve the spread of tensile yielding during loading and will provide experimental data to verify recommended provisions eliminating the TFY checks and incorporating the tension yielding response in the calculation of the true M_{yc}.

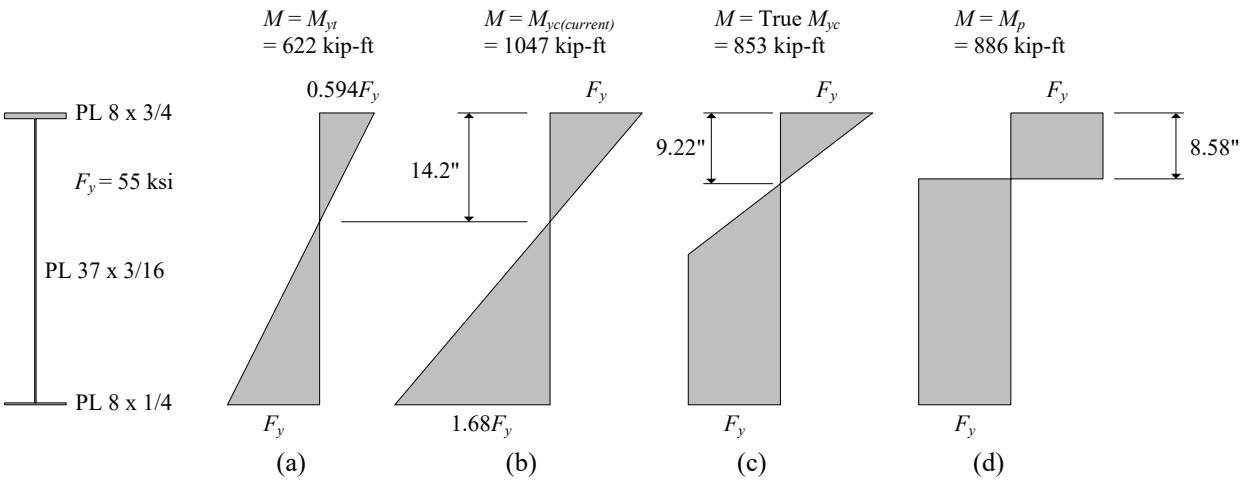

Figure 3: Stress profiles based on AISC (2016) versus the true stress profile of a homogeneous I-section.

Table 4: Design matrix of new TFY test specimens*.

Test #	Web	L_b	Flange PL†	Web PL	c	K	KL_b/r_t	C_b	R_{pc} or R_{pg}
9	Slender/Compact	16	8x3/4 8x1/4	37x3/16	4.00	1.00	88	1.75	1.04
10	Slender/Compact	19	8x3/4 8x1/4	37x3/16	4.75	1.00	105	1.75	1.04
11	Slender/Compact	22	8x3/4 8x1/4	37x3/16	5.51	1.00	121	1.75	1.04
12	Slender/Compact	5	8x3/4 8x1/4	37x3/16	1.47	1.17	32	1.00	1.04

* Specimen designs conducted assuming a static yield strength of the plates◘ of F_y = 60 ksi; units for L_b are in ft., all other dimensions are in units of inches

† $b_{fc}/2t_{fc}$ = 5.33, all tests

3. Test Configuration

The test set-up is specially designed to minimize incidental restraint. Incidental restraint can have a measurable impact on large-scale experimental LTB beam results by increasing the capacity beyond that based on the intended boundary conditions (Ziemian 2010). The test configuration in effect fully releases or rigidly restrains selected degrees-of-freedom at the bearing, load, and bracing points. Load-height effects at the actuator can make the calibration of design equations to observed specimen behavior less direct. Therefore, to eliminate any potential load-height effects, the lateral and torsional displacements are restrained at the bearing and load points. The design of the test setup is based largely on the concepts discussed in SSRC Technical Memorandum No. 9 on flexural testing (Ziemian 2010). Fig. 4 is a photograph of the overall test setup. The white member is the test specimen, the blue members constitute the bracing reaction system, and the load frame is painted grey. The specific loading and support fixtures and bracing details are discussed below.

Figure 4: Perspective view of the test configuration.

3.1 Boundary Conditions

Roller boundary conditions are provided at the support fixtures, and are symmetric about the mid-length of the test specimen. Longitudinal translation is permitted via a lubricated roller pack composed of four 2.5-in. diameter solid steel rods. A 100-kip load cell (Load Cell Central, Milan, Pennsylvania, Model: LPSW-B-100K LB) is located above each roller pack. Transverse displacement is restrained at the bearing location through Watt's linkage braces discussed in the following section. The three rotational degrees of freedom are released through Polytetrafluoro-ethylene (PTFE) lined GX45T Thrust Loading Spherical Plain (AST Bearings, Parsippany, New Jersey, Model: GX45T). The PTFE thrust bearings allow free in-plane rotation due to bending and free out-of-plane rotation associated with flange warping and/or lateral bending. The spherical bearing is seated in a counter-bored plate on top of the load cell. Fig. 5 provides a conceptual drawing of the bearing detail used for all tests as well as a photograph of the final bearing detail.

In addition, a PTFE spherical thrust bearing is located at the point of load application. Furthermore, load-point bracing was provided through a Watt's linkage system. Fig. 6 shows the conceptual and implemented boundary condition at a load point.

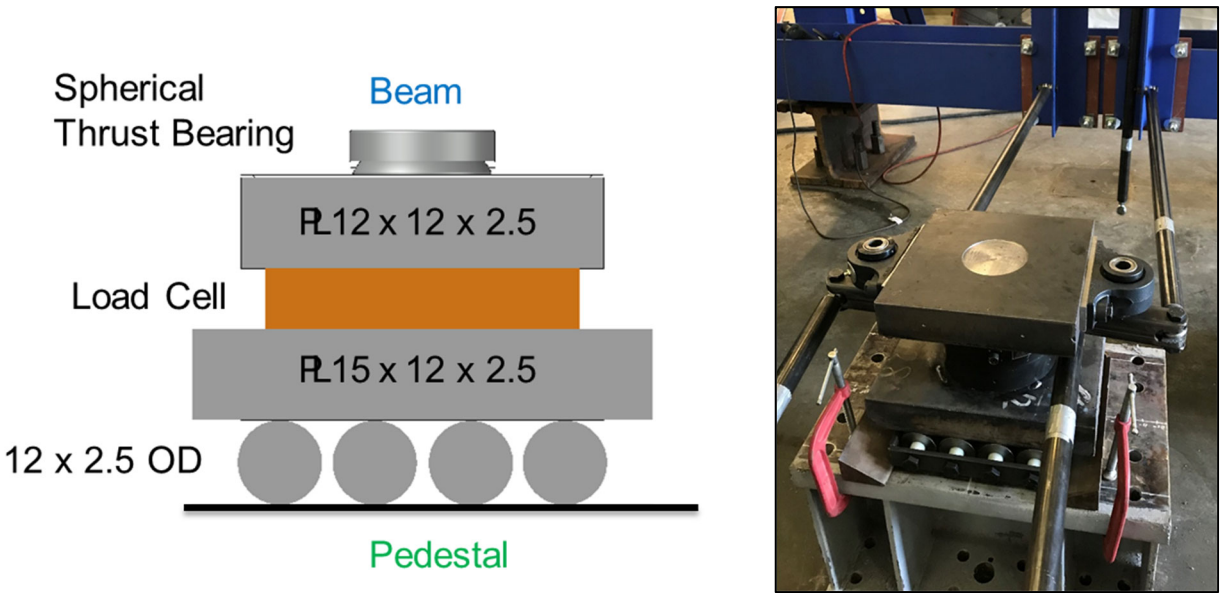

Figure 5: Bearing boundary condition detail, concept (left) and implementation (right). The spherical bearing is excluded in the photo to show the counter-bore. Additionally the roller pack is chocked in the photo to prevent incidental movement while installing the test specimen.

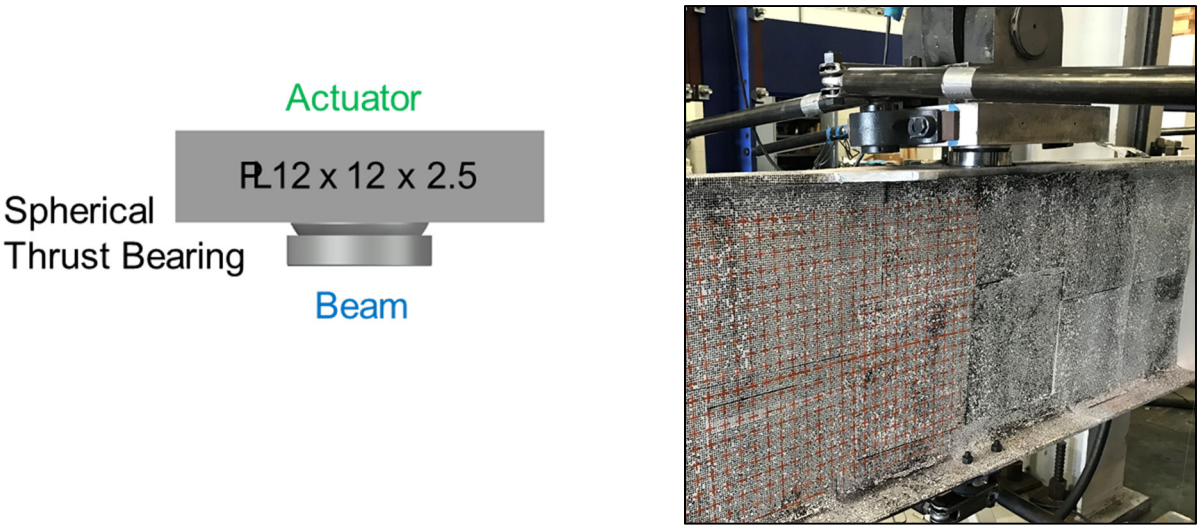

Figure 6: Load point boundary condition detail, concept (left) and implementation (right).

3.2 Bracing System

The bracing system is designed using a mechanical system known as a Watt's linkage. The Watt's linkages restrain displacements perpendicular to the girder webs, while allowing free translation in the longitudinal and vertical directions. This type of bracing system has been used previously by Yarimci et al. (1967), Smith et al. (2013) and others. In the current tests, the system is comprised of two tie rods with ball joint rod ends attached to the stiff reaction frames (painted blue in Fig. 4) and a center link. The center link is free to rotate about a vertical axis and transfers lateral forces through a cylindrical mechanical bearing referred to as a flange block. Fig. 7 illustrates the ability of the linkage system to prevent deflections in the direction perpendicular to the girder webs, i.e., the horizontal direction in the figure, under large longitudinal displacements (i.e., displacements in the vertical direction in the figure). In addition, girder vertical deflections (i.e., deflections into

and out of the page in the figure) are accommodated by the rotation of the center link about a vertical axis.

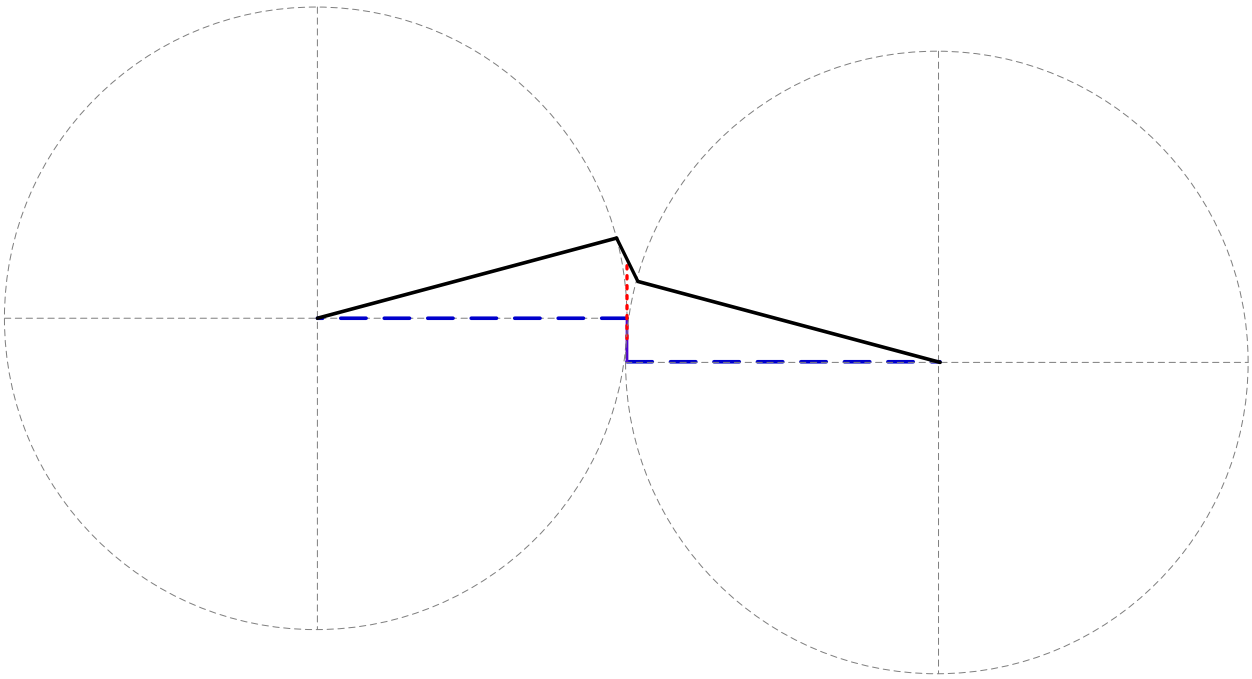

Figure 7. Illustration of a Watt's Linkage movement under a large deflection along the axis of the test specimen. The heavy dashed blue lines represent the initial condition, the solid black lines represent a deformed condition, and the red dashed line illustrates the path of the brace point between the two conditions.

The Watt's linkage system does an excellent job of releasing incidental constraint. Several additional unique features added to the designed bracing system include:

1) Each end of the tie rods is threaded. Left-hand threads are used on one end and right-hand threads are used on the other. This allows for quick length adjustments via rotation of the bar, without having to unbolt the ends, allowing for fine adjustments to ensure the test specimen is plumb at each brace point. In addition, jam nuts are used to ensure the rod length does not change while under load.
2) A rail system is implemented to allow for a rapid implementation of various unbraced lengths and bracing configurations. The tie rods are bolted to vertical WT members containing a series of holes to accommodate varying specimen heights. The bracing reaction frame is composed of wide flange rails that extend the entire length of the test setup. Lindapter friction-based connections (UCC Steelwork Connections Inc., Syracuse, New York, Items: LB075 L, LA075 M, LCW075 M, and ¾"x4.5" BNW) are used to connect the vertical WT sections. Each WT can easily slide along the rails to accommodate a range of specimen unbraced lengths.
3) Each brace point, including the friction-based Lindapter connection, is designed to accommodate a transverse force of 20 kips. To achieve this capacity, while releasing the vertical rotations at the girder flanges for the Watt's linkage system, a Timken Type E Tapered Roller Bearing Housed Unit, E-4BF-TRB-1 7/16 (The Timken Company, North Canton, Ohio, UPC: 053893549767) flange block is employed. At the load application and bearing locations, pillow blocks with a different housing but using the same internal Timken cylindrical bearing are selected. To prevent pull out, the OD of the stem of the center-link is match machined to

the ID of the bearing for a press-fit connection. Additionally, four set screws bear on flats on the center-link stem.

4. Test Specimens

The test specimens are fabricated by prominent metal building manufacturers, and are representative of main frame members in typical metal building frames. The web-to-flange welds are minimum size single-sided fillet welds. Both flanges are fabricated from rolled bar stock, while the web was cut from coil. In addition, each specimen has double-sided stiffener plates at all the brace points to control cross-sectional distortion.

Detailed measurements of the initial imperfect geometry are recorded for each specimen, including the plate thickness and width of both flanges and the web, flange sweep, flange tilt, flange warpage, web off-center, and web out-of-flatness. All thickness measurements are conducted using a paint thickness compensating ultrasonic thickness tester, a high precision angle finder, machined straight edges, high tension-test fishing line, and calipers. Initial residual stress measurements are performed on each specimen.

4.1 Specimen Geometry

All specimens are measured to determine their imperfect geometry in the no load condition, after being installed and plumbed at all the brace points within the test setup. Table 5 provides the measured plate dimensions for the elastic LTB verification test described in Section 5.

Table 5: Average measured plate sizes. All unit in inches.

b_{ft}	t_{ft}	b_{fc}	t_{fc}	h	t_w
4.968	0.313	4.968	0.313	29.983	0.246

The measured compression flange sweep and web out-of-flatness for this test are shown in Figs. 8 and 9. The other geometric imperfection measurements are not shown for brevity.

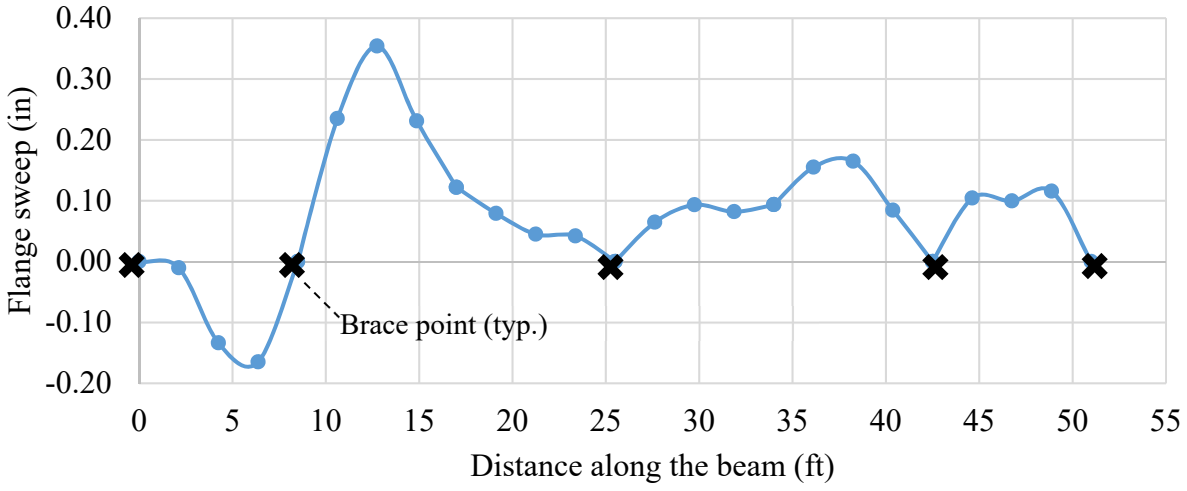

Figure 8: Compression flange sweep.

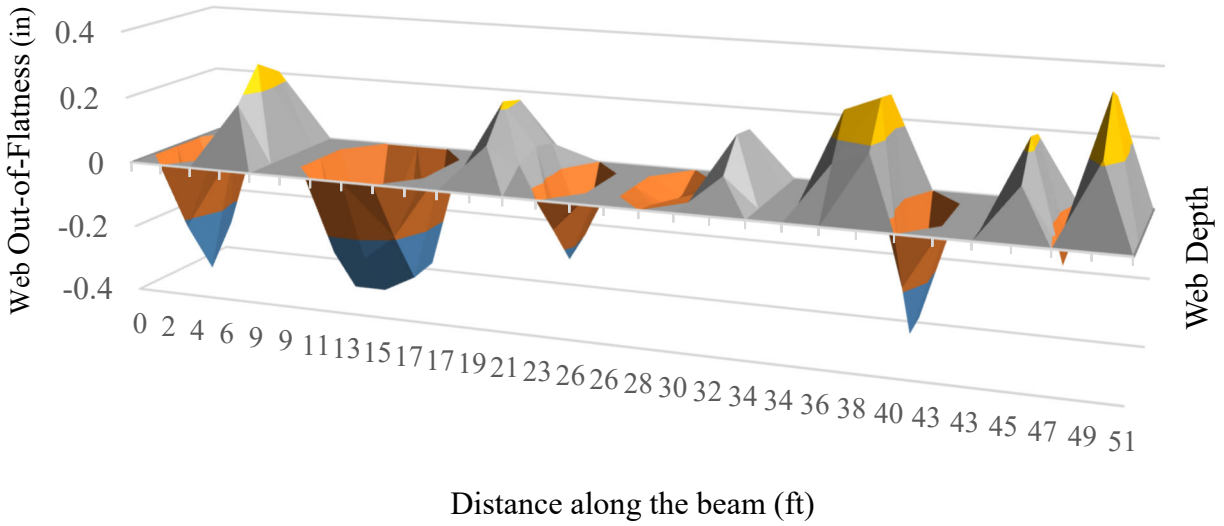

Figure 9: Web out-of-flatness. The color contours highlight intervals of 0.2 inches.

4.2 Material Properties

A minimum of three ASTM E8/E8M-16 (ASTM 2016) rectangular plate tensile coupons are tested for each mill heat and plate thickness. The testing protocol also follows ASTM E8/E8M-16 (ASTM 2016). Based on the test data, the numerical and analytical calculations conducted in Section 5 use an average flange yield of 58.2 ksi and web yield of 61.9 ksi.

Pre-test FEA solutions were conducted using one-half of a best fit to residual stresses measured in typical metal building frame members by Prawel (1974), as discussed by Subramanian et al. (2017). A final analysis of each specimen is conducted based on residual stresses measured in accordance with ASTM E837 (ASTM 2013).

5. Validation of Test Setup

To ensure the effectiveness of the displacement and rotational releases in the test setup, the braces were removed from at the adjacent brace points on each side of the actuator in Test 5 (Table 3). This positions the strength of this modified specimen well within the elastic LTB range. The modified specimen was loaded up to elastic buckling twice in tests referred to as 5E.A and 5E.B. The resulting peak load from the load-deflection curves can be compared directly to the theoretical elastic LTB resistance defined within the AISC Specification and to the capacity from finite element models. The load versus horizontal displacement of the flanges also can be employed to obtain an experimental estimate of the theoretical elastic buckling strength via Southwell, Meck, and Massey plots (Mandal and Calladine, 2002).

Fig. 10 shows the elevation view of the Specimen 5 and the resulting moment diagram at the elastic LTB load condition. The AISC Commentary Eq. C-F1-2b gives a moment gradient factor of C_b = 1.38 for the critical unbraced lengths on each side of the mid-span for this loading condition, whereas AISC Eq. F1-1 gives 1.33. Both Eqs. C-F1-2b and F1-1 are intended as lower-bound estimates. Eq. C-F1-2b tends to give a larger and more accurate lower bound (Slein et al., 2018). The elastic LTB effective length factor is obtained rigorously as K = 0.82 using the SABRE2

software (Toğay et al. 2020). Note that a conservative value of K = 0.87 is obtained using the approximate procedure developed by Nethercot and Trahair (1976).

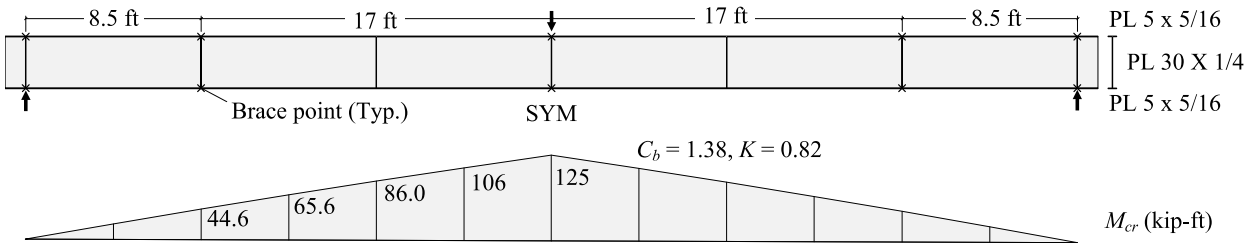

Figure 10. Elastic LTB validation test geometry, showing nominal cross-section plate dimensions, and moment diagram at the theoretical elastic LTB load level.

5.1 Elastic LTB Validation to Analytical and Numerical Solutions

The elastic specimen is a doubly symmetric section with a noncompact web according to the current (2016) AISC *Specification*. Since the specimen is loaded with a moment gradient, with a large KL_b/r_t of 0.82(17 ft)(12 in/ft)/1.082 in = 154, the weight of the beam and bracing components becomes nontrivial. Fig. 11 shows the loads applied to the beam and the corresponding moment diagram prior to zeroing the load cells. This includes the influence of the self-weight, the weight of the stiffeners, the weight of the flange blocks, half of the weight of the tie rods, the weight of the center links, and the miscellaneous hardware. Note that the additional load from the flange blocks and stiffeners at the interior brace point is only 37.6 lbs after disconnecting the rod ends. The other bracing hardware remained mounted to the beam. In addition, a small load is applied by seating of the actuator on the spherical bearing at the top of the girder at the mid-span, prior to zeroing the load cells. All of the above loads are added to the sum of the loads measured at the load cells to calculate the girder moment diagram at the peak load level.

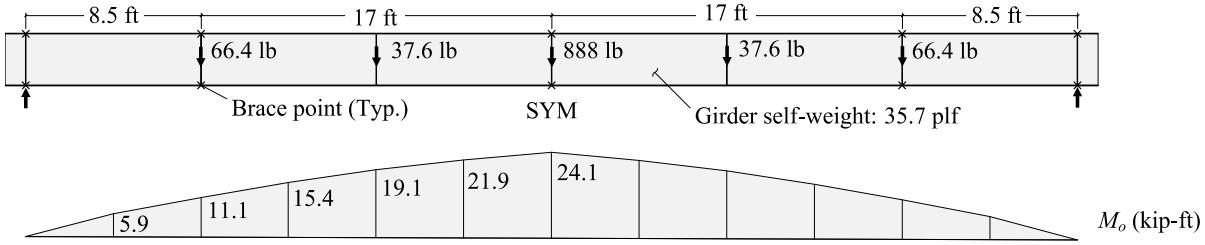

Figure 11: Loads and moments prior to starting data acquisition.

This specimen was used subsequently for the inelastic LTB Test 5; therefore, yielding of the section was monitored from several strain gauges during the two elastic tests. Loading was halted immediately when the horizontal displacement began to dramatically increase with a small increase in load and yielding was starting to initiate at locations subjected to the largest strains. Therefore, the maximum loads achieved in the experimental tests do not necessarily correspond to the true maximum load capacity of the specimen in this elastic LTB test configuration.

It is important to note that due to stable elastic post-buckling response in the governing lateral-torsional buckling mode, the specimen is potentially able to develop a maximum load capacity slightly larger than the elastic critical load. This is due to the large LTB slenderness for this elastic

LTB testing arrangement. The extent to which this elastic post-buckling strength is realized depends upon the extent of the early yielding that occurs due to the combined effects of the girder loads, initial geometric imperfections, and initial residual stresses. These aspects are discussed further in the following.

The two elastic LTB tests were halted at peak loads, including the initial 888 lb at the midspan, of 9401lb and 9366 lb. The corresponding maximum girder moments were 132.6 kip-ft and 132.8 kip-ft. Fig. 12 and Table 6 compare the test strengths to the theoretical elastic LTB strength curve from AISC (2016), the maximum load capacity obtained from a geometric and material nonlinear shell finite element analysis with imperfections and residual stresses included, using ABAQUS (Simulia, 2018) (commonly referred to in the literature as a GMNIA solution), and an elastic eigenvalue buckling FEA solution obtained from SABRE2 (Toğay et al. 2020), based on thin-walled open-section beam theory (commonly referred to as an ELBA solution). The GMNIA and ELBA solutions correspond the specific LTB effective length of $KL_b = (0.82)(17\text{ ft}) = 13.9$ ft, but are indicated by horizontal lines in the plot to clearly illustrate the corresponding moment levels. The yield moment to the compression flange, M_{yc} = 401.2 kip-ft, is employed as a factor to normalize the results in Fig. 12 and in subsequent result presentations.

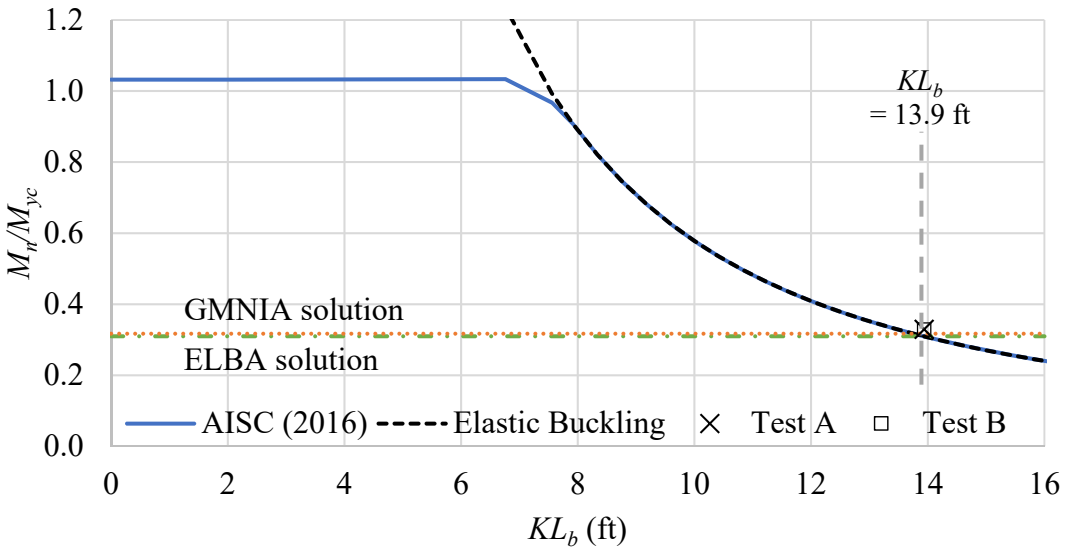

Figure 12: Test results shown in relation to the theoretical elastic LTB strength curve from AISC (2016) and to GMNIA and ELBA numerical solutions.

Table 6: Comparison of experimental capacity to analytical and numerical solutions.

Elastic Test	$M_{test}/M_{n.AISC}$	$M_{test}/M_{cr.ELBA}$	$M_{test}/M_{n.GMNIA}$
5E.A	1.06	1.06	1.04
5E.B	1.06	1.06	1.04

The nominal LTB capacity curve in Fig. 12 is calculated using the applicable AISC (2016) Section F4 provisions. In the elastic LTB region of the curve, the nominal capacity is the same as the theoretical elastic buckling strength, expressed as

$$M_{cr} = \frac{C_b \pi^2 E S_{xc}}{\left(KL_b / r_t\right)^2} \sqrt{1 + 0.078 \frac{J}{S_{xc} h_o} \left(KL_b / r_t\right)^2} \tag{2}$$

where C_b is the moment gradient factor, E is the elastic modulus, S_{xc} is the section modulus, L_b is the unbraced length of the critical section, r_t is the radius of gyration, J is the St. Venant torsion constant, and h_o is the distance between the flange centroids.

It should be noted that several refinements to the calculations shown directly in AISC (2016) Section F4 are necessary to achieve the accuracies shown in Fig. 12 and Table 6:

1) The C_b factor should be calculated using Eq. C-F1-2b from the AISC (2016) Commentary. This equation commonly provides a slightly larger value compared to Eq. F1-1. Slein et al. (2018) report on the results from parametric studies that show Eq. C-F1-2b provides a more accurate lower-bound estimate of exact C_b values for a comprehensive range for I-section members. The ratio of the C_b from Eq. C-F1-2b to Eq. F1-1 is 1.38/1.33 = 1.04 for Tests 5E.A and 5E.B.
2) The radius of gyration should be calculated as

$$r_t = \frac{b_{fc}}{\sqrt{12\left(\frac{h_o}{d} + \frac{1}{6} a_w \frac{h^2}{h_o d}\right)}} \tag{3}$$

where

$$a_w = \frac{h_c t_w}{b_{fc} t_{fc}} \tag{4}$$

rather than by the simplified equation

$$r_t = \frac{b_{fc}}{\sqrt{12\left(1 + \frac{1}{6} a_w\right)}} \tag{5}$$

For the Test 5 girder, the value of r_t from Eq. (3) is 1.082 compared to 1.072 from Eq. (5). The ratio of the elastic buckling resistance from Eq. (2) using Eq. (3) for r_t versus Eq. (5) is 1.02. This ratio tends to be larger for relatively shallow I-section members with relatively thick flanges. Eq. (3) gives a value close to the "exact" r_t = 1.084 for doubly symmetric I-sections given by AISC (2016) Eq. F2-7. Eq. (3) is specified in Section F4 of the 2010 AISC Specification; however, this equation was changed to Eq. (5) as a simplification in the 2016 AISC Specification.

The combined effect of the above ratios is (1.04)(1.02) = 1.06, which results in $M_{test}/M_{n.AISC}$ in Table 6 being 1.12 if the less accurate C_b and r_t equations are employed.

It should be noted that if the end restraint effects are neglected in the above AISC calculations, by using an LTB effective length factor of $K = 1.0$ in addition to the above approximations, $M_{n.AISC}$ = 79.1 kip-ft and the ratio of $M_{test}/M_{n.AISC}$ in Table 6 becomes 1.68, i.e., the AISC calculation is 68 % conservative.

If one employs $E = 29{,}500$ ksi for the structural steel, which is close to the mean for the modulus of elasticity with a small coefficient of variation, rather than the nominal value of $E = 29{,}000$ ksi, the ratios $M_{test}/M_{n.AISC}$ and $M_{test}/M_{n.ELBA}$ in Table 3 become 1.04.

As noted above, the GMNIA solution is capable of capturing a physical capacity in Tests 5E.A and 5E.B that is slightly larger than the theoretical elastic LTB strength. This is due to the stable elastic post-buckling response of the girder. The contributions from elastic post-buckling strength are negligible for most practical LTB slenderness values; however, given the large slenderness in these elastic LTB tests, strengths larger than the theoretical elastic LTB resistance are possible. Fig. 13 shows the mid-span moment versus the compression flange lateral deflection from the GMNIA solution, a geometric nonlinear (linear elastic material) analysis with imperfections (referred to in the literature as a GNIA solution) and the ELBA solution obtained from SABRE2.

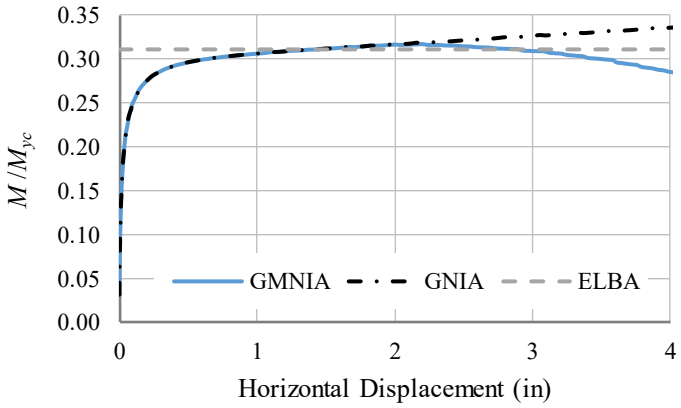

Figure 13: Load-horizontal displacement curves from ABAQUS GMNIA and GNIA solutions and comparison to the ELBA solution from SABRE2.

Nevertheless, it can be observed that, as the theoretical elastic critical moment is approached, the compression flange lateral displacement increases at a rapidly increasing rate, both in the full nonlinear (GMNIA) and the geometrically nonlinear (GNIA) shell FEA solutions. The corresponding rapid increase in the compression flange lateral bending strains results in the onset of yielding within the compression flange, resulting in a limit load in the GMNIA solution. This behavior was observed within the experiment, except that the magnitude of the lateral deflections were significantly smaller in the experiment compared to the shell FEA solutions. The second-order amplifications of the girder lateral displacements and twists in the experiment matches well with the theory, as demonstrated in Section 5.2 below. One can surmise that when the rate of change of the compression flange lateral displacements increases abruptly, the girder is very close to its maximum capacity.

Fig. 14 shows the buckling mode obtained from the SABRE2 ELBA solution. The lighter-shaded arrows indicate the concentrated loads on the girder while the darker-shaded arrows indicate the

beam FEA displacement and rotational constraints. The deformed shape at the peak load and within the post-peak range of the response in the GMNIA and GNIA solutions is of a similar form to this deformed shape.

An additional ELBA solution was conducted using ABAQUS with the same shell finite element discretization employed for the above GMNIA and GNIA solutions. The total mid-span moment at the elastic critical load level is 122.8 kip-ft versus 124.6 kip-ft in the SABRE2 ELBA solution. The ratio between these solutions is 122.8/124.6 = 0.986. In addition, SABRE2 is capable of performing an elastic nonlinear buckling analysis (ENBA), in which the influence pre-buckling vertical displacements is accounted for in the eigenvalue buckling solution. Furthermore, SABRE2 has capabilities for inelastic linear buckling analysis (ILBA) and inelastic nonlinear buckling analysis (INBA), which account for inelastic stiffness reductions derived from the AISC LTB resistance equations. For the 5E.A and 5E.B tests, the critical mid-span moment from the ENBA solution is only 0.1 % larger than the ELBA result. In addition, the 5E.A and 5E.B tests are well within the elastic LTB range. Therefore, the ILBA and INBA solutions are identical to the ELBA and ENBA solutions, respectively.

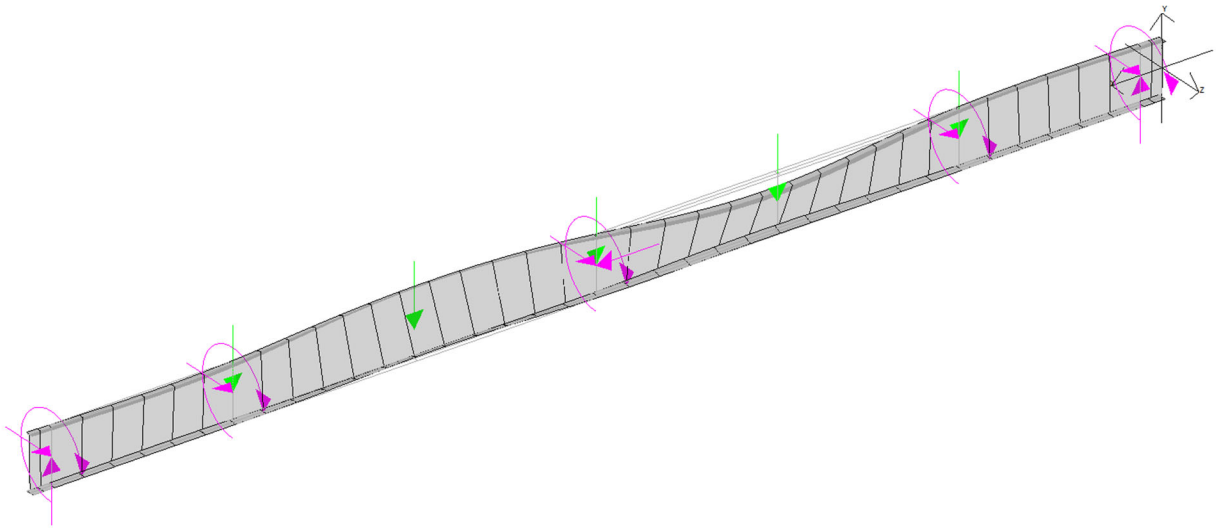

Figure 14: Refined buckling solution from thin-walled open-section beam theory in SABRE2 (Toğay et al. 2020).

5.2 Experimental Estimation of Elastic Buckling Load by Southwell, Meck, and Massey plots

As a final evaluation of the effectiveness of the releases in the test setup, measured displacements and loads are used to generate Southwell, Meck, and Massey plots for Tests 5E.A and 5E.B. These plots allow estimation of the elastic critical moment of the specimen, M_{cr}. Mandal and Calladine (2002) discuss the effectiveness and theoretical underpinnings of these different types of plots for beam lateral-torsional buckling problems. Each of the methods plot a variation of load versus displacement, then use the inverse of the slope of the plotted line to estimate M_{cr}.

The Southwell plot for LTB is generated by plotting the lateral displacement of the compression flange, u, versus u/M. The lateral displacement is monitored using a linear string potentiometer (Celesco Transducers, Toronto, Ontario, Model: PT1A-50-UP-500-M6-SG). The lateral displacement is measured at the location in the critical unbraced length where the compression flange lateral displacements are expected to be largest. The method is not sensitive to the specific

selected location. It is important to note that the specimen is preloaded up to at least 60% of the expected buckling load, then unloaded, until the displacement returns to the same value after loading and unloading. This ensures that all the boundary conditions are well seated. The maximum moment at the mid-span is calculated as

$$M = PL/4 + M_o \tag{6}$$

where P is the summation of load cell readouts at the end supports, L is the distance between the end supports, and M_o is the mid-span value shown in Fig. 11. Fig. 15 shows the generated Southwell plot for Test 5E.A. The result for Test 5E.B is similar.

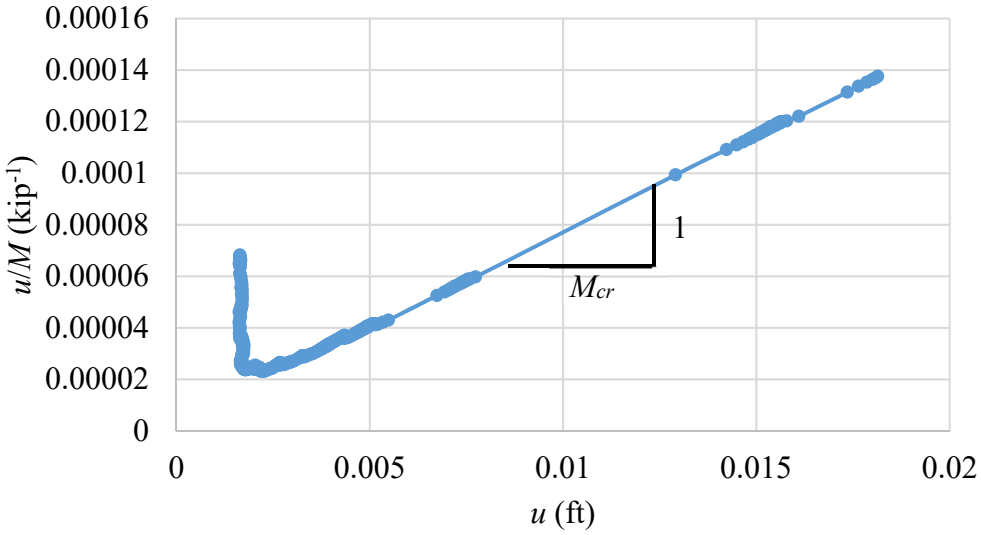

Figure 15: Southwell plot for Test 5E.A.

The Meck plot is similar to the Southwell plot but also considers the twist of the cross-section. During the elastic test the tension flange in Tests 5E.A and 5E.B had negligible out-of-plane motion; therefore, the twist of the cross-section is proportional to the lateral displacement of the compression flange. The Meck plot takes M_{cr} as the Euclidian norm of, α, the inverse slope of u/M versus φ and, β, the inverse slope of φ/M versus u, i.e.,

$$M_{cr} = \sqrt{\alpha\beta} \tag{7}$$

Figs. 16 and 17 show the values for α and β. The Massey plots take M_{cr} as the Euclidian norm of, α, the inverse slope of φ/M^2 versus φ and, β, the inverse slope of u/M^2 versus u, shown by Fig. 17.

There is some complexity that is not captured by these methods due to the fact that the specimen is not flexurally and torsionally simply supported. As such, the second-order amplifications of the compression flange lateral deflection, u, and the twist, φ, strictly do not have the same mathematical form as that of a simply-supported column. However, the methods agree reasonably well with each other. In the limit that the moment approaches the theoretical elastic buckling

moment, it appears that the simple assumption for the form of the second-order amplification of the displacements, embedded within the Southwell, Meck and Massey plots, applies reasonably well. The results from the maximum loading applied in the experiment and from each of the methods are summarized in Table 6.

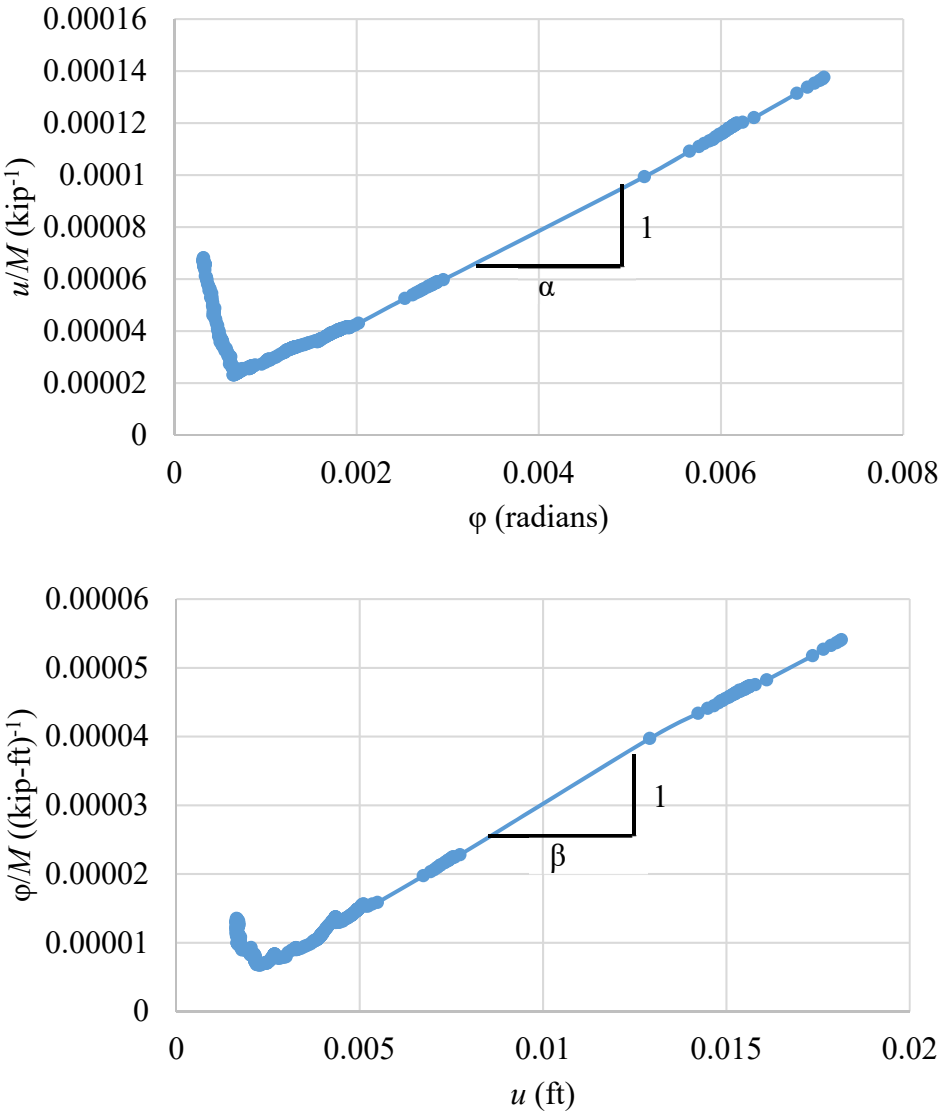

Figure 16: Meck plots for Test 5E.A.

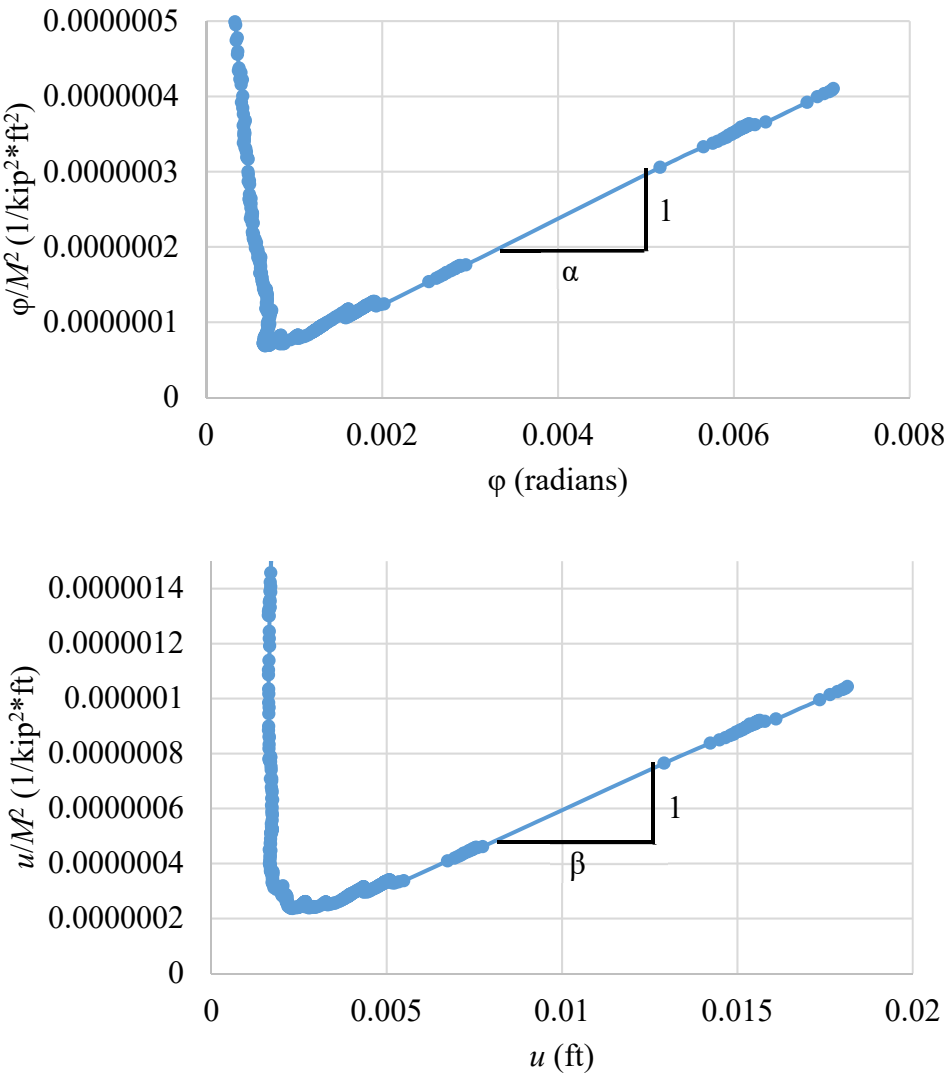

Figure 17: Meck plots for Test 5E.A.

Table 6: Comparison of maximum moment applied in the experiment, M_{test}, to experimental estimates of the theoretical elastic critical moment, M_{cr}.

M_{test} (experiment) and M_{cr} values (kip-ft)			
Experiment	Southwell	Meck	Massey
132.6	138.0	136.6	130.6

6. Conclusions

Incidental restraint can have a measurable impact on experimental LTB test results. Details of a testing setup that minimizes this incidental constraint are presented. To validate the effectiveness of the testing setup, two elastic tests were conducted and compared to various analytical and numerical predictions, as well as to experimental estimates of the theoretical elastic critical moment. The results show good agreement between the experiments and the predictions, demonstrating the minimization of incidental constraint.

Acknowledgments

The authors would like to acknowledge MBMA, AISC, and AISI for their generous support of this research; American Buildings Company, BlueScope Buildings North America, and Schulte Building Systems for their generous donations of the test specimens; AISC and NUCOR Fastener Division for material and fastener donations; and Dr. Tom Murray of Virginia Tech for serving as a senior advisor to the project. They would also like to thank the Georgia Tech Structural Engineering Laboratory staff and other GT personnel for their many contributions to the project.

References

AASHTO (2017). *AASHTO LRFD Bridge Design Specifications*, 8th Edition, American Association of State and Highway Transportation Officials, Washington, D.C.

AISC (2016). *Specification for Structural Steel Buildings*, ANSI/AISC 360-16, American Institute of Steel Construction, Chicago, IL.

ASTM Standard E8/E8M, 2016, "Standard Test Methods for Tension Testing of Metallic Materials," ASTM International, West Conshohocken, PA, 2003, DOI: 10.1520/E0008_E0008M-16A, www.astm.org.

ASTM Standard E837, 2013, "Standard Test Method for Determining Residual Stresses by the Hole-Drilling Strain-Gage Method," ASTM International, West Conshohocken, PA, 2003, DOI: 10.1520/E0837-13A, www.astm.org.

Mandal, P. and Calladine, C.R. (2002). "Lateral-Torsional Buckling of Beams and the Southwell Plot," *International Journal of Mechanical Sciences*, 44(12), 2557-2571.

Nethercot, D.A. and Trahair, N.S. (1976). "Lateral Buckling Approximations for Elastic Beams," *Structural Engineering*, 54(6), 197-204.

Prawel, S.P., Morrell, M.L., and Lee, G.C., Bending and buckling strength of tapered structural members, Weld. Res. Suppl. 53 (1974) 75–84.

Simulia (2018). Abaqus Standard User Manual 2018, Dassault Systems. < https://www.3ds.com/products-services/simulia/services-support/support/documentation/> (January 17, 2020).

Slein, R.S., Jeong, W.Y, and White, D.W. (2018). "A Critical Evaluation of Moment Gradient (C_b) Factor Calculation Procedures for Doubly and Singly Symmetric I-Section Members," Research Report, School of Civil and Environmental Engineering, Georgia Institute of Technology, Atlanta, GA.

Smith, M. D., A. K. Turner and C.-M. Uang (2013). "Experimental study of cyclic lateral-torsional buckling of web-tapered I-beams". *Department of Structural Engineering University of California*, San Diego: 268 pp.

Subramanian, L. and White, D.W. (2017). "Resolving the Disconnect between Lateral Torsional Buckling Experimental Tests, Test Simulations and Design Strength Equations," *Journal of Constructional Steel Research*, 128, 321-334.

Subramanian, L., Jeong, W.Y., Yellepeddi, R. and White, D.W. (2018). "Assessment of I-Section Member LTB Resistances Considering Experimental Tests and Practical Inelastic Buckling Design Calculations," *Engineering Journal,* AISC, 55(1), 15-44.

White, D.W. and Jeong, W.Y. (2020). *Design of Frames Using Nonprismatic Members***,** AISC/MBMA Design Guide 25, 2nd Edition, American Institute of Steel Construction and Metal Building Manufacturers Association, (to appear).

White, D.W. and Jung, S.-K. (2004). "Unified Flexural Resistance Equations for Stability Design of Steel I-Section Members – Uniform Bending Tests," Structural Engineering, Mechanics and Materials Report No. 28, School of Civil and Environmental Engineering, Georgia Institute of Technology, Atlanta, GA, 127 pp.

White, D.W. and Kim, Y.D. (2004). "Unified Resistance Equations for Stability Design of Steel I-Section Members – Moment Gradient Tests," Structural Engineering, Mechanics and Materials Report No. 26, School of Civil and Environmental Engineering, Georgia Institute of Technology, Atlanta, GA, 149 pp.

Toğay, O., Slein, R., Jeong, W.Y. and White, D.W. (2020). "SABRE2," <white.ce.gatech.edu/sabre> (January 17, 2020).

Yarimci, E., Yura, J. A., and Lu, L. W., "Techniques for testing structures permitted to sway, Experimental Mechanics, Vol. 7, No. 8, August 1967, Reprint" (1967). Fritz Laboratory Reports. Paper 112. http://preserve.lehigh.edu/engr-civil-environmental-fritz-lab-reports/112

Ziemian, R.D. (Ed.), Guide to Stability Design Criteria for Metal Structures (Sixth Ed.), John Wiley & Sons, Inc., Hoboken, NJ (2010)